$MoSe_2$ quantum dots modified hole extraction layer enables binary organic solar cells with improved efficiency and stability

Hong Lian,[‡a,b] Mingao Pan,[‡c] Jinba Han,[a] Xiaozhe Cheng,[a] Jiaen Liang,[c] Wenqiang Hua,[d] Yongquan Qu,[a] Yucheng Wu,[a] Qingchen Dong,*[a,b] Bin Wei,*[b] He Yan,*[c] and Wai-Yeung Wong*[e]

In this paper, we demonstrate a solution-processed $MoSe_2$ Quantum Dots/PEDOT:PSS bilayer hole extraction layer (HEL) for non-fullerene organic solar cells (OSCs). It is found that introduction of $MoSe_2$ QDs can alter the work function and phase separation of PEDOT:PSS, thus affecting the morphology of active layer and improving the performance of OSCs. The $MoSe_2$ QDs/PEDOT:PSS bilayer HEL can improve the fill factor (FF), short-circuit current density (J_{sc}) and power conversion efficiency (PCE) of OSCs based on different active layers. The best PCE of up to 17.08 % was achieved based on a recently reported active layer binary system named SZ2:N3, which is among the highest reported value to date for OSCs using 2D materials as the interface modifier. Our study indicates that this simple and solution-processed $MoSe_2$ QDs/PEDOT:PSS bilayer thin film could be a potential alternative HEL to the commonly used PEDOT:PSS conducting polymer.

Introduction

Bulk heterojunction (BHJ) organic solar cells (OSCs) have received notable scientific and industrial interest because of their merits of being light weight, low-cost, easy-flexibility, and the promise for mass production by roll-to-roll print process.[1-6] To date, due to the continued progresses in the exploration of low band-gap polymer donors and non-fullerene acceptor, the maximum power conversion efficiencies (PCE) of the single-junction and tandem non-fullerene OSCs have reached over 17%, respectively, allowing them one step closer to commercial application.[7,8] In addition to the advances in synthesizing novel materials, interface engineering is currently recognized as one of the most efficient strategies to boost device efficiency and stability. In particular, the hole extraction layer (HEL) between the anode and active layer plays a key role in anode modification, energy level alignment, charge collection and morphology controlling, *etc*.[9-11] Therefore, various kinds of HEL are being used to further improve the performance of OSCs. The presently reported HEL were mainly transition-metal oxides, metal sulfides, conducting polymers, conjugated polyelectrolytes (PCPDTK$_{0.50}$H$_{0.50}$-TT, PCPDTffPhSO$_3$K), graphene oxides, etc.[12,14] Among, the conducting conjugated polymer poly(3,4-ethylenedioxythiophene):poly(styrenesulfonate) (PEDOT:PSS) has been widely used as a HEL in organic optoelectronic devices, because of its appropriate work function, excellent conductivity, high optical transparency and compatibility with the solution processes.[15-18] However, as is well known, the high acidity and hygroscopicity of PEDOT:PSS can corrode the indium tin oxide (ITO) electrode, which will eventually degrade the performance and long-term stability of OSCs. Furthermore, the poor electron blocking ability and anisotropy in the conductivity of PEDOT:PSS films usually lead to serious leakage current and inhomogeneous charge extraction in some locations. In terms of the above issues, the main solutions focus on substituting PEDOT:PSS with transition-metal oxides, such as molybdenum oxide (MoO_3), vanadium oxide (Va_2O_5), nickel oxide (NiO), and tungsten oxide (WO_3), *etc*.[19-24] Unfortunately, these materials are usually fabricated by high vacuum techniques, which are not only high-cost and have complicated processing steps but also not compatible with the roll-to-roll manufacturing technology. Another effective approach is to insert an interfacial modifier between the HEL/ITO interface for improving the interfacial contact quality and reducing electrical losses.[25]

Many efforts have been devoted to the HEL/ITO interface engineering of single-junction OSCs. Solution-processed transition metal dichalcogenides (TMDs) (MoS_2, WS_2, TaS_2 and $NbSe_2$, *etc*.) have recently attracted considerable attention due to their unique optical and electronic properties. In particular, single- and few-layered TMDs or TMDs quantum dots (QDs) have been used to

[a]*MOE Key Laboratory of Interface Science and Engineering in Advanced Materials, Taiyuan University of Technology, 79 Yingze West Street, Taiyuan, 030024, China. E-mail: dongqingchen@tyut.edu.cn.*

[b]*MOE Key Laboratory of Advanced Display and System Applications, Shanghai University, Shanghai, 200072, China. E-mail: bwei@shu.edu.cn.*

[c]*Department of Chemistry and Hong Kong Branch of Chinese National Engineering Research Center for Tissue Restoration & Reconstruction, Hong Kong University of Science and Technology, Clear Water Bay, Kowloon, Hong Kong. China. E-mail: hyan@ust.hk.*

[d]*Shanghai Advanced Research Institute, Chinese Academy of Sciences, 201210, China.*

[e] *Department of Applied Biology and Chemical Technology and Research Institute for Smart Energy (RISE), The Hong Kong Polytechnic University, Hung Hom, Hong Kong, China.*

[‡]*These people contribute equally to this work.*

modify HEL, or within the active layer of OSCs to enhance device performance and stability.[26-32] In 2013, Gu et al. proposed the integration of chemically exfoliated solution-processed MoS_2 nanosheets and $NbSe_2$ nanoplates as efficient anode buffer layer for performance optimization of OSCs.[33,34] The as-reported PCE with the PTB7:$PC_{71}BM$ system as the active layer is superior to that obtained by using traditionally vacuum deposited e-MoO_3. In 2014, Le et al. reported the use of spin-coated ultraviolet ozone (UVO)-treated, sonication exfoliated MoS_2 nanosheets as an interlayer between the anode and the PEDOT:PSS in a P3HT:$PC_{61}BM$-based OSC.[35] The device exhibited enhanced stability without degradation of its photovoltaic performance compared to the device employing only PEDOT:PSS. It is noteworthy that the mechanism of performance improvement based on MoS_2 nanosheets as interfacial modifiers for HEL has never been systematically explored yet.

In this work, we firstly reported a solution-processed composite HEL within $MoSe_2$ QDs and PEDOT:PSS to improve the device performance and stability of OSCs. Meanwhile, the working principle of two-dimensional (2D) $MoSe_2$ QDs as HEL interface modifier in OSCs was studied thoroughly for the first time. Compared to the device with only PEDOT:PSS, the $MoSe_2$ QDs/PEDOT:PSS bilayer HEL efficiently reduced the charge recombination and enhanced the charge extraction and transport due to its well-matched work function (WF) and superior conductivity. We also investigated the stability of OSCs without and with $MoSe_2$ QDs, and found that the stability of OSC with $MoSe_2$ QDs is dramatically improved due to the separation of ITO and PEDOT:PSS caused by insertion of $MoSe_2$ QDs. The champion device based on $MoSe_2$ QDs/PEDOT:PSS showed a PCE of 17.08 %, which is the highest value among OSCs with 2D materials as the interface modifier so far. The excellent PCE of $MoSe_2$ QDs/PEDOT:PSS based device is attributed to its higher short-circuit current density (*Jsc*), which is mainly derived from the superior conductivity and suitable work function of $MoSe_2$ QDs/PEDOT:PSS.

Results and discussion

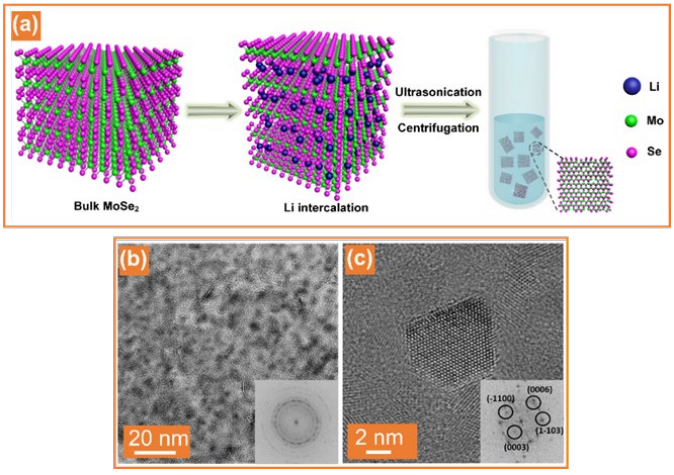

Fig. 1. (a) Schematic diagram of preparation process of monolayer $MoSe_2$ QDs using a lithium intercalation and ultrasonication method. The magnified area shows the layered structure of $MoSe_2$ QDs, with the chalcogen atoms (Se) in purple and the metal atoms (Mo) in green. (b) TEM and (c) HR-TEM images measured for the $MoSe_2$ QDs.

The $MoSe_2$ QDs were synthesized through lithium intercalation and ultrasonication method as depicted in Fig. 1a. It is worth noting that $MoSe_2$ QDs prepared by most methods suffer from intrinsic structural defects, which are detrimental to device performance. The crystal structure of the layered $MoSe_2$ QDs is presented in Fig. 1a. It is a typical sandwiched structure and the interlayer effect is relatively weak and easy to peel off, leading to specific anisotropic mechanical and electrical properties. In addition, some *in situ* derived structural defects in $MoSe_2$ QDs are usually difficult to avoid. Transmission electron microscopy (TEM) and high-resolution TEM (HR-TEM) images were used to measure the crystal structures of $MoSe_2$ QDs. Fig. 1b is a conventional bright field TEM image showing many crystalline QDs. The dark contrasts correspond to Bragg contrasts and the inserted selected area electron diffraction (SAED) pattern reveals the presence of $MoSe_2$ (hexagonal, a=b=0.329 nm and c=1.293 nm). To further analyze the atomic structure of individual $MoSe_2$ QDs, we measured the HR-TEM image of a single $MoSe_2$ QD (as presented in Fig. 1c), revealing that these as-prepared $MoSe_2$ QDs possess high crystallinity.[36] The fast Fourier transform (FFT) of the QD (inset of Fig. 1c) is in perfect agreement with a [-2110] projection of the $MoSe_2$ structure. To investigate the composition of the resultant $MoSe_2$ QDs, the corresponding energy-dispersive X-ray spectroscopy (EDS) elemental mapping images were measured, as shown in Fig. S1. The results indicate that Mo (green) and Se (yellow) elements were uniformly distributed over the entire QDs.

It was pointed out in previous literatures that high-temperature annealing could tune the WF of HEL, improving the performance of OSCs.[37,39] However, the underlying mechanisms have not yet been studied. Herein, the $MoSe_2$ QDs film was annealed at high-temperature and its structural composition was confirmed by the X-ray photoelectron spectra (XPS), as depicted in Fig. S2a, S2b and S2c. Notably, the characteristic peaks around 235.7 and 232.2 eV, as well as the peaks at 59.5 and 58.7 eV, corresponding to the Mo^{6+} $3d_{5/2}$ and Mo^{6+} $3d_{3/2}$, and Se^{4+} $3d_{5/2}$ and Se^{4+} $3d_{3/2}$, respectively, were also observed. This indicates that Mo and Se elements in $MoSe_2$ QDs are partially oxidized to MoO_3 and SeO_2 species. Generally, SeO_2 seldom exists in HEL, given that it has a low sublimation temperature.[36] The Mo^{6+} 3d spectrum exhibits another two contributes, located at respectively 235.2 and 231.9 eV, which can be assigned to O-Mo-Se band due to the participated lattice oxygen atoms.[40] It is deduced that the O incorporation not only could partially fill the Se vacancies and passivate the structural defects, but lead to a change of interfacial energy level alignment (change n-type $MoSe_2$ to p-type), which is beneficial to device efficiency and stability (see detail in Supplementary Information and Fig S2d). Then, we studied the morphology and optical properties of the thin films. The as-prepared $MoSe_2$ QDs solution and PEDOT:PSS were spin-coated onto ITO substrates, respectively. Fig. S3(a-c) shows the atomic force microscopic (AFM) images of ITO substrate, PEDOT:PSS and $MoSe_2$ QDs thin films as coated on ITO, respectively. It can be observed distinctly that the root-mean-square (R_q) surface roughness of ITO, ITO/PEDOT:PSS and ITO/$MoSe_2$ QDs are 3.70, 2.62 and 1.27 nm, respectively, indicating that $MoSe_2$ QDs can decrease the RMS of ITO and then result in a smaller leakage current. The normalized UV-vis absorption spectrum of post heat-treated $MoSe_2$ QDs film is shown in Fig. S3d.

It can be seen clearly that $MoSe_2$ QDs film may absorb some amount of UV light, whereas not impacting the absorption of active layer in solar cells. This is highly desirable for the device performance and stability optimization of OSCs.[41,42] The overall transmittance spectra of ITO, ITO/PEDOT:PSS and ITO/$MoSe_2$ QDs/PEDOT:PSS are presented in Fig. S3e. It can be found that the transmittance of ITO/PEDOT:PSS thin film is higher than pure ITO in the range of 300-800 nm. With the introduction of $MoSe_2$ QDs into PEDOT:PSS, the transmittance is nearly unchaged. This may be attributed that the energy distributions of both PEDOT:PSS and $MoSe_2$ QDs/PEDOT:PSS have been changed due to the different interfaces between ITO and HEL, which facilitates the enhancement of light interference and thus the increase of transmittance.[43] This is in agreement with the analyses of Fig. S3d, and demonstrates that the $MoSe_2$ QDs layer can server as an effective interlayer in traditional ITO/PEDOT-based OSCs. In addition, the effect of $MoSe_2$ QDs on the morphology of the active layer was also measured by the AFM, as shown in Fig. S3f and S3g. Compared to R_q of PEDOT:PSS/BHJ (6.65 nm), the surface roughness of $MoSe_2$ QDs/PEDOT:PSS/BHJ increases to 6.94 nm after the insertion of $MoSe_2$ QDs. Such a change is likely caused by a positive interaction between $MoSe_2$ QDs and PEDOT:PSS, which is instrumental in forming solid contact with BHJ, thus preventing BHJ from spreading to HEL. The slightly increased R_q is beneficial for modulating phase separation of BHJ, increasing device efficiency and stability.[44] The discrepancy of R_q is ascribed to the different surface energies of HEL or ITO, which can be quantitatively calculated by the water contact angle. The contact angle of different materials measured with water and ethylene glycol (EG) as testing liquids (equal volume of liquids for each test) are displayed in Fig. 2. The calculation details are described in the Supplementary Information and Table S1-S3. The $MoSe_2$ and $MoSe_2$/PEDOT:PSS films exhibit water and EG contact angles lower than the ITO and pristine PEDOT:PSS. It was pointed out in literatures that the surface energy of HEL has a marked impact on the orientation of BHJ, that is, the face-on orientation dominates at high surface energy, while the edge-on orientation is easier to form at low surface energy.[45] The surface energy of ITO, $MoSe_2$, PEDOT and $MoSe_2$/PEDOT:PSS films are 68.8, 70.0, 85.5 and 89.0 mN m^{-1}, respectively. The corresponding interfacial energies of $MoSe_2$ and PEDOT:PSS, $MoSe_2$/PEDOT:PSS and PM6:Y6 are calculated to be 7.5 and 128.4 mN m^{-1}, respectively, which are much higher than ITO and PEDOT (4.4 mN m^{-1}), and PEDOT:PSS and PM6:Y6 (121.0 mN m^{-1}), indicating that the insertion of $MoSe_2$ QDs can not only alter the morphology of PEDOT:PSS and BHJ but also facilitate the phase separation in PEDOT:PSS and BHJ, which benefits the face-on orientation of BHJ and enhances the device performance.

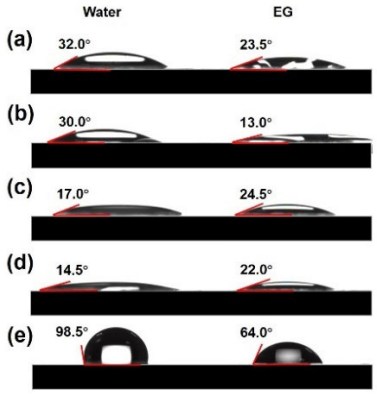

Fig. 2. Water and EG contact angles of various materials: (a) ITO, (b) $MoSe_2$ QDs, (c) PEDOT:PSS, (d) $MoSe_2$ QDs/PEDOT:PSS, (e) PM6:Y6.

The OSCs with standard structure were fabricated based on a typical binary blend of PM6:Y6 and state-of-the-art BHJ systems of SZ2:N3 to investigate the influence of $MoSe_2$ QDs/PEDOT:PSS as a composite HEL on device performance. Schematic device structure and the chemical structures of the components in the active layer are presented in Fig. 3a and 3b. Since the WF of HEL plays an important role in controlling the carrier injection properties, the WFs of PEDOT:PSS and $MoSe_2$ QDs/PEDOT:PSS thin films coated on the ITO substrates were determined by ultraviolet photoelectron spectroscopy (UPS). The corresponding UPS spectra are shown in Fig. 3c. The secondary electron cut-off ($E_{cut\text{-}off}$) values of the PEDOT:PSS and $MoSe_2$ QDs/PEDOT:PSS films are measured to be 16.2 and 16.0 eV, respectively. Therefore, the WF of $MoSe_2$ QDs/PEDOT:PSS film was determined to be 5.2 eV (WF = 21.22 eV-$E_{cut\text{-}off}$-E_{onset}), which lies slightly higher than that of PEDOT:PSS (5.0 eV).[46] The energy diagram of the OSCs with different HELs is illustrated in Fig. 3d. All of the energy levels of ITO, PM6, Y6, SZ2, N3, PFN-Br and Al refer to the values as reported in the literature.[47,48] It can be observed clearly that, the insertion of $MoSe_2$ QDs can pull up the HOMO energy level of HEL, which is favorable for efficient hole extraction and reducing charge recombination near the anode. Moreover, the $MoSe_2$ QDs/PEDOT:PSS HEL can also better block the electron transport compared to the one with only PEDOT:PSS, resulting in a smaller leakage current. The increase of WF is ascribed to the formation of Mo^{6+} species due to the oxidation of selenium vacancies and edge termination, indicating that $MoSe_2$ QDs/PEDOT:PSS HEL has a p-type conductive mechanism.[49]

The thickness of $MoSe_2$ QDs film is optimized by changing the spin-coating speed to obtain an optimal value (see Fig. S4a and Table S4). Fig. 4 displays the current density–voltage (J–V) characteristics of the fabricated devices and their detailed photovoltaic performances including J_{sc}, open-circuit voltage (V_{oc}), fill factor (FF) and PCE are summarized in Table 1. Clearly, after inserting $MoSe_2$ QDs as the surface modifier, the J_{sc} and FF of OSCs with $MoSe_2$ QDs/PEDOT:PSS composite HEL realize an obvious increase compared to the control cell. In PM6:Y6 system, the champion device based on composite HEL exhibited a maximum PCE value of 16.08 % with J_{sc} of 25.84 mA cm^{-2}, V_{oc} of 0.83 V, FF of 74.69% and series resistance (R_s) of 3.63 Ω cm^2 while the control cell with PEDOT:PSS HEL exhibited a maximum PCE value of 15.48 % with J_{sc} of 24.68 mA cm^{-2}, V_{oc} of 0.84 V, FF of 74.29% and R_s of 7.94

Ω cm^2. It indicates that this simple and solution-processed $MoSe_2$ QDs/PEDOT:PSS bilayer thin film could contribute to boosting device efficiency. The impressive device performance makes $MoSe_2$ QDs/PEDOT:PSS bilayer thin film a promising HEL candidate for near future high-efficiency optoelectronic devices. The maximum EQE value of OSC with $MoSe_2$ QDs/PEDOT:PSS as HEL is approximately 80 % and the calculated J_{sc} is 25.32 mA/cm^2, which is consistent with the value extracted from the *J–V* measurements with deviation of only 5%. In SZ2:N3 system, these results are in agreement with those of PM6:Y6. Fig. 4c and 4d shows the *J–V* curves and EQE spectra of control cell and $MoSe_2$ QDs/PEDOT:PSS-based cell. Evidently, compared with the control cell, the J_{sc} and FF values of

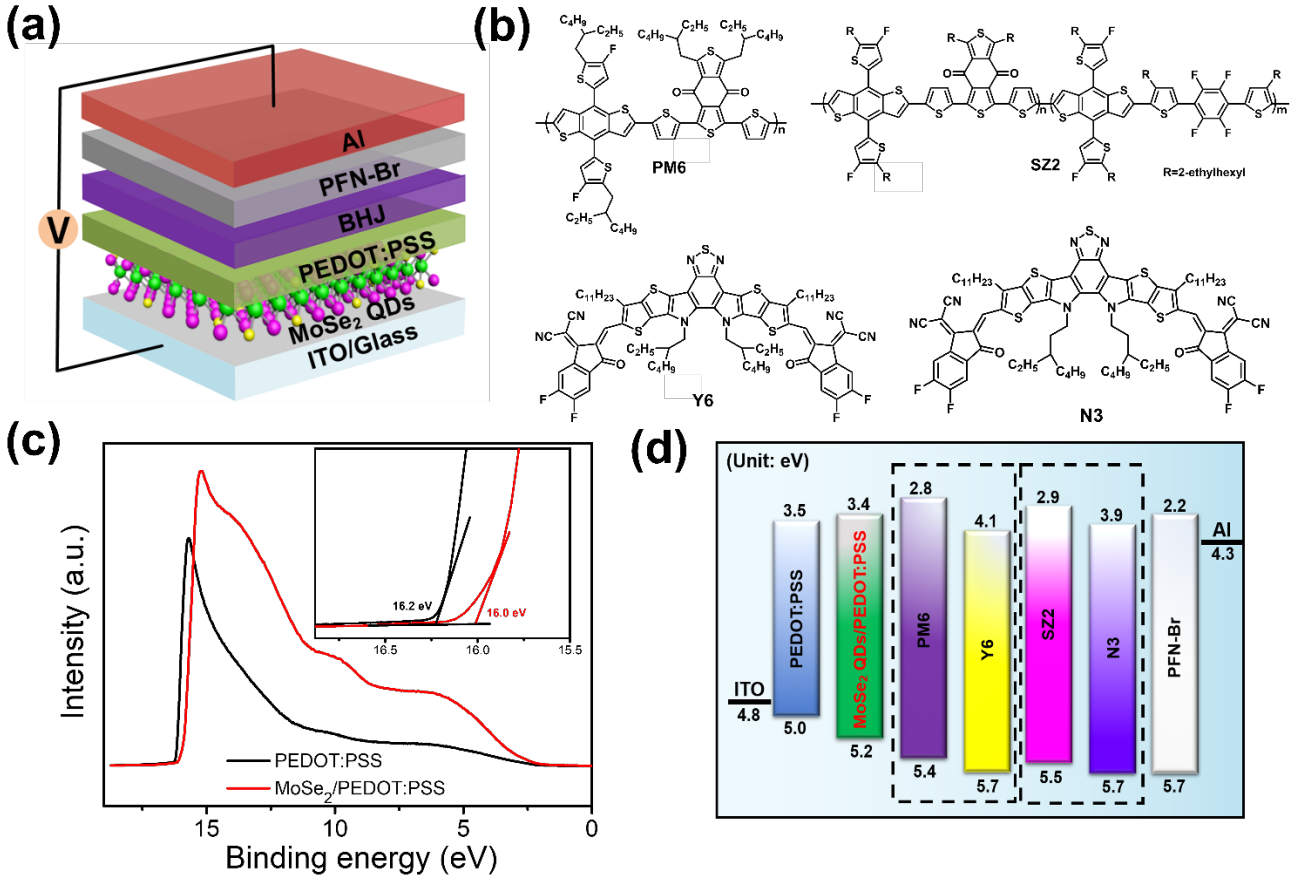

Fig. 3. (a) Schematic device structure inserted with $MoSe_2$ QDs. (b) The chemical structures of BHJ. (c) UPS spectra of the cut-off region of the PEDOT:PSS and $MoSe_2$/PEDOT:PSS. (d) Energy level diagram of the OSCs.

the $MoSe_2$ QDs/PEDOT:PSS-based cell increase from 25.22 to 25.63 mA/cm^2 and 77.11 to 77.52%, respectively. According to the EQE spectra, the corresponding calculated J_{sc} value of the EQE spectra increases from 25.02 to 25.21 mA/cm^2, which agree well with the J_{sc} in *J–V* characteristics, showing a good reliability of our results. Especially, the OSC based on SZ2:N3 with $MoSe_2$ QDs/PEDOT:PSS as HEL yielded a maximum PCE of 17.08%, while the control cell only showed a PCE of 16.53%. In order to ensure the reproducibility and reliability of the PCE, the histogram of PCE based on SZ2:N3 using different HEL are plotted in Fig. S5. It is obvious that PCE values of SZ2:N3 based solar cells is in normal distribution. The average PCE of PEDOT:PSS and $MoSe_2$/PEDOT:PSS based solar cells are 16.28 ± 0.14% and 16.89 ± 0.12%, respectively, with a reasonably narrow standard deviation, which further indicates the good reproducibility and reliability of the PCE of corresponding OSCs. Recent reports of 2D materials as the interface modifier in OSCs are classified in Table S5. The PCE of our OSCs and those of the previously reported OSCs with 2D materials have been compared in Fig. 4e. [33-35,50-55] The PCE value in our work is the highest value among OSCs with 2D materials as the interface modifier so far.

In order to investigate the effect of $MoSe_2$ QDs on charge generation and dissociation processes, the photocurrent density (J_{ph}) and exciton dissociation probabilities *P(E,T)* versus effective voltage (V_{eff}) are measured and plotted, as shown in Fig. 4c and S6a.The charge extraction/collection values of these devices are extracted from the J_{ph}–V_{eff} curves, suggesting that $MoSe_2$ QDs/PEDOT:PSS-based cell shows more efficient charge extraction/collection capability compared with control device. Apart from the factors of charge generation and dissociation, the charge recombination loss of OSCs is also a key parameter for analysis of the enhancement mechanism of PCE. Fig. S6b and S6c depict the variation of J_{sc} and V_{oc} versus the light intensity (*I*) for all cells with *I* ranging from 5 to 100 mW cm^{-2}. Herein, the α values based on $MoSe_2$ QDs/PEDOT:PSS HEL are significantly higher than that of control cell (0.967), demonstrating that the insertion of $MoSe_2$ QDs reduce the bimolecular recombination of cell (see detail in ESI). Furthermore, the transport characteristics of cells were

measured to gain an insight of the mechanism responsible for the PCE enhancement. In fact, it is worth mentioning that $MoSe_2$ QDs/PEDOT:PSS-based cell exhibits the higher α value (0.989), which was very close to 1, indicating a negligible bimolecular recombination process. In case of V_{oc} versus I, V_{oc} is proportional to ln I. From Figure S6c, it is observed that the minimum slope of $MoSe_2$ QDs/PEDOT:PSS-based cell is 1.04 kT/q, meanwhile, the slope of control cell is 1.14 kT/q. The results imply that insertion of $MoSe_2$ QDs can effectively suppress monomolecular recombination originated from traps and defects, which devotes to improving the performance of OSCs.

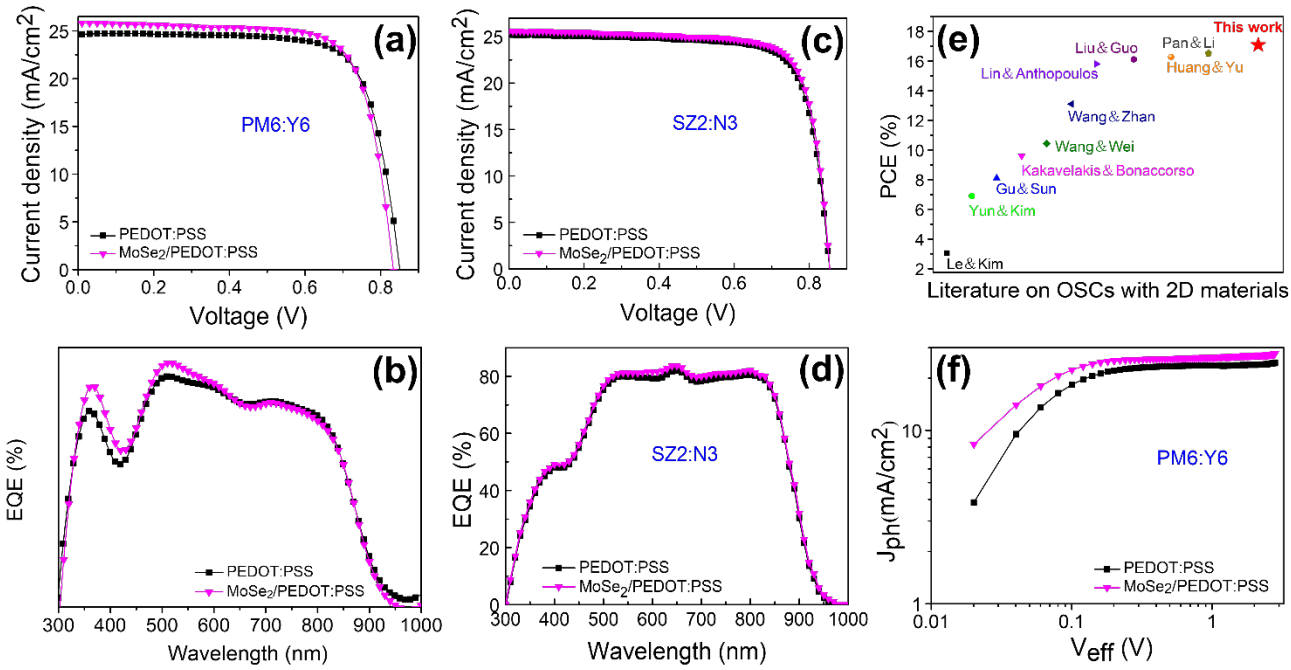

Fig. 4. (a) *J–V* and (b) EQE curves of PM6:Y6 solar cells. (c) *J–V* and (d) *EQE* curves of SZ2:N3 solar cells. (e) A comparison of the performance of previously reported OSCs with 2D materials. (f) J_{ph}-V_{eff} curves of PM6:Y6 solar cells.

Table 1. Summary of device performances of OSCs with or without $MoSe_2$ QDs.

BHJ	Description	J_{sc} [mA cm^{-2}]	V_{oc} [V]	FF [%]	PCE [%]	R_s [Ω·cm^2]	J_{cal} [mA cm^{-2}]
PM6:Y6	PEDOT:PSS	24.68 (24.56±0.2)	0.84(0.84±0.002)	74.29(74.26±1.08)	15.48 (15.18±0.23)[a]	7.94	24.05
	$MoSe_2$/PEDOT:PSS	25.84 (25.68±0.3)	0.83(0.84±0.003)	74.69(74.31±1.30)	16.08 (15.75±0.24)[a]	3.63	25.32
SZ2:N3	PEDOT:PSS	25.22(25.21±0.3)	0.85(0.84±0.003)	77.11(77.09±0.09)	16.53 (16.32±0.12)[a]	8.36	25.00
	$MoSe_2$/PEDOT:PSS	25.63(25.72±0.3)	0.86(0.85±0.003)	77.52(76.34±1.42)	17.08 (16.86±0.20)[a]	4.23	25.23

[a]Average PCE with standard deviations were obtained from 10 devices

The dark *J–V* characteristics of the cells are plotted in Fig. S7a, in which the device with $MoSe_2$ QDs/PEDOT:PSS HEL enables a lower leakage current and a higher rectification ratio, and thereby a reduced R_s in the cells, as shown in Table 1. Additionally, we fabricated two hole only devices with the device structures of ITO/$MoSe_2$ QDs/PEDOT:PSS/PM6:Y6/MoO_3/Al and ITO/PEDOT:PSS/PM6:Y6/MoO_3/Al, respectively, and then employed space charge limited current (SCLC) method for the evaluation of hole only transport properties. The hole mobility is evaluated by Mott–Gurney equation:[56]

$$J_{sc}=\frac{9}{8}\varepsilon_r\varepsilon_0\mu_h\frac{V_{eff}^2}{d^2} \quad (1)$$

where ε_r is the relative dielectric constant (assuming to be 3), ε_0 is the permittivity of free space (8.85× 10^{-12} F m^{-1}), μ_h is the hole mobility, V_{eff} is the effective voltage and d is the film thickness of active layer (150 nm). As shown in Fig. S7b, the hole mobility (μ_h) of $MoSe_2$ QD/PEDOT:PSS-based cell and the control cell is calculated to be 2.26×10^{-4} and 6.30×10^{-5} cm^2 $V^{-1}s^{-1}$, respectively. Evidently, OSCs with $MoSe_2$ QDs/PEDOT:PSS as HEL exhibit higher conductivity compared with control cell owing to its unique chemical structure and physical properties, which agrees well with the results of conductivities as measured by the Van der Pauw four-probe conductivity technique (Table S6). Since the lower frequency arc is associated with the charge recombination behavior, electric impedance spectroscopy (EIS) measurement is often used to analyze interface properties in OSCs.[57,58] Nyquist plots of the impedance spectroscopy (IS) of the control cell and ITO/$MoSe_2$ QDs/PEDOT:PSS-based cells at zero bias under dark condition are

shown in Fig. S8a. It can be seen obviously that, compared to control cell, the $MoSe_2$ QDs/PEDOT:PSS-based cells show smaller semicircles, indicating the lower transport resistance and interfacial barrier between the ITO and $MoSe_2$ QDs/PEDOT:PSS. The reduced transport resistance is favorable for charge transporting and extraction, which benefits the increase of J_{sc} and FF values. Fig. S8b shows the PL emission spectra of ITO/PM6, ITO/PEDOT:PSS/PM6 and ITO/$MoSe_2$ QDs/PEDOT:PSS/PM6 thin films, respectively. The $MoSe_2$ QDs/PEDOT:PSS/PM6 film exhibits a much lower PL quenching efficiency (9 %) than the PEDOT:PSS/PM6 film (20%), indicating that the exciton dissociation in $MoSe_2$ QDs/PEDOT:PSS/PM6 film are more efficient than PEDOT:PSS/PM6, which results in higher EQE and J_{sc} for the corresponding OSCs. The corresponding PL intensity of active film with $MoSe_2$ QDs was significantly enhanced as compared to that of without $MoSe_2$ QDs, primarily due to diminished exciton quenching effect after insertion of $MoSe_2$ QDs.[59] The PL measurement again prove that the embedded $MoSe_2$ QDs can facilitate the charge transport and thus contribute to boosting the efficiency of OSCs. Fig. S8c displays the PL intensity decay profiles obtained for PEDOT:PSS/PM6:Y6 and $MoSe_2$ QDs/PEDOT:PSS/PM6:Y6 thin films. It is obvious that the lifetime of excitons in $MoSe_2$ QDs/PEDOT:PSS device (0.840 ns) is shorter than that in PEDOT:PSS device (0.962 ns), which is mainly attributed to the efficient exciton dissociation and charge collection of $MoSe_2$ QDs/PEDOT:PSS. So, we can infer that the introduction of $MoSe_2$ QDs can increase the charge extraction rate and thus reduce charge recombination, which is beneficial to the enhancement in J_{sc} of the devices.

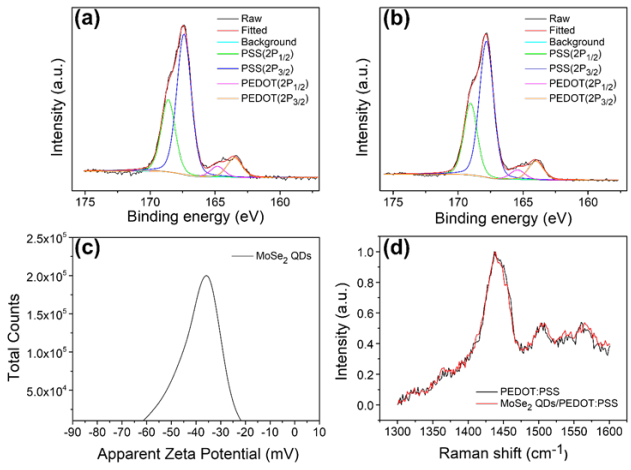

Fig. 5. S 2p XPS spectra measured for (a) the pristine PEDOT:PSS and (b) $MoSe_2$ QDs/PEDOT:PSS thin films. (c) Zeta potential of $MoSe_2$ QDs dispersions. (d) Raman spectra of PEDOT:PSS and $MoSe_2$ QDs/PEDOT:PSS films.

In order to further deeply explore the intrinsic working mechanism of $MoSe_2$ QDs in OSCs, we measured the XPS spectra for the pristine PEDOT:PSS and $MoSe_2$ QDs/PEDOT:PSS thin films to examine the change of the chemical and electronic properties of PEDOT:PSS before and after the insertion of $MoSe_2$ QDs. Fig. 5 shows that there are two characteristic S 2p peaks with the binding energy at 167.5 eV and 163.5 eV, respectively, in the S 2p XPS spectrum of the pristine PEDOT:PSS film, which are assigned to the S species of PSS and PEDOT, respectively.[60,61] In pristine PEDOT:PSS films, PEDOT was attached by insulating PSS via columbic interaction which promotes the dissolution of PEDOT in solution, whereas hinders the charge transport in solid films of device. However, when $MoSe_2$ QDs and PEDOT:PSS form bilayer, the ratio of PSS to PEDOT gradually decreased from 6.98 of the pristine PEDOT:PSS to the 6.88 of $MoSe_2$ QDs/PEDOT:PSS. This reveals the interfacial interaction between $MoSe_2$ QDs and PEDOT:PSS, which results in a phase separation between PEDOT and PSS and then causes aggregation of conducting PEDOT.[62] Hence, the insertion of $MoSe_2$ QDs helps remove partial insulated PSS with strong acidity and hygroscopicity, which enhances the conductivity of the PEDOT:PSS and device stability. To gain more insights, we investigated the zeta potential of $MoSe_2$ QDs (Fig. 5c), which is measured to be -38.8 mV. Consequently, 2D $MoSe_2$ QDs with the negatively charged surface can promote the aggregation of PEDOT to form a more regular chain-type morphology, thus weaken the shield effect of PSS on PEDOT and improve the electron conductivity of PEDOT:PSS.[63] There is no denying that the conformational change of PEDOT is concerned with the conductivity of the PEDOT:PSS film. Therefore, the Raman spectra were conducted to examine whether the improvement of conductivity is due to the conformational change of PEDOT chains from coil (benzoid structure) to linear (quinoid structure) or expanded-coil structure or not. It is noted that no obvious change was observed between 1400 and 1500 cm^{-1} denoting C_α=C_β double bond in the PEDOT thiophene ring (Fig. 5d), [64,65] implying that the enhanced conductivity of the PEDOT:PSS film was not owing to the conformational change of PEDOT chains. Taking the above phenomena into account, we proposed a reasonable mechanism about the conductivity enhancement of PEDOT:PSS film induced by $MoSe_2$ QDs. From the chemical structures,[66] one can conclude that the PSS chain is of much heavier molecular weight than PEDOT chain, thereby more positively charged PEDOT molecules are attached to PSS chains. As a result of the positive charge on PEDOT, the repulsions between the PSS anions were weakened, allowing the PEDOT to form a coiled or core-shell structure with insulated PSS surrounded.[62] Furthermore, the negatively charged $MoSe_2$ QDs can attract the PEDOT and reject PSS, accelerate the aggregation of PEDOT in the core-shell structure, promote more conductive PEDOT chains to escape from PSS encirclement and boost up the conductivity of the whole PEDOT:PSS layer.

Finally, grazing-incidence wide-angle X-ray scattering (GIWAXS) was carried out to study the molecular packing and crystallinity orientation of the PM6:Y6. Fig. S9(a–c) depict the 2D GIWAXS images of the PM6:Y6 based on different HEL and the corresponding profiles both along the in-plane (IP, dotted line) (q_{xy}) and the out-of-plane (OOP, solid line) (q_z) directions. The profiles of PM6:Y6 films with different HEL exhibit strong (100) diffraction peak in IP direction and (010) diffraction peak in OOP direction, indicating the co-existence of face-on and edge-on molecular orientation in the BHJ. It could be clearly observed clearly from **Fig. S9c** that PEDOT:PSS based PM6:Y6 film exhibits a strong (010) peak in OOP direction at 1.74 $Å^{-1}$. When introducing $MoSe_2$ QDs interlayer, the (010) peak resulting from the π–π stacking can be observed in OOP direction at 1.76 $Å^{-1}$. According to the formulas of $d = 2\pi/q$ and $L = 2\pi K/\Delta q$, where q is the peak position, K is the

Scherrer constant (~ 0.9), Δq is the half maximum of each peaks, the π-π stacking distance (d-spacing) and the coherence length L are determined to be (0.360 nm and 0.217 nm) and (0.352 and 0.403 nm), respectively, for PEDOT:PSS/PM6:Y6 and $MoSe_2$ QDs/PEDOT:PSS/PM6:Y6. [68] So, it is clearly that the π-π stacking distance of the PM6:Y6 film based on bilayer HEL is smaller than the PM6:Y6 film based on PEDOT:PSS HEL, which is favorable for intermolecular electron hopping. In addition, the coherence length of PM6:Y6 film based on bilayer HEL is larger than that based on PEDOT:PSS. Note that the increased *L* corresponds to higher crystallinity and better phase separation of BHJ, leading to increased charge transport and decreased bimolecular recombination.

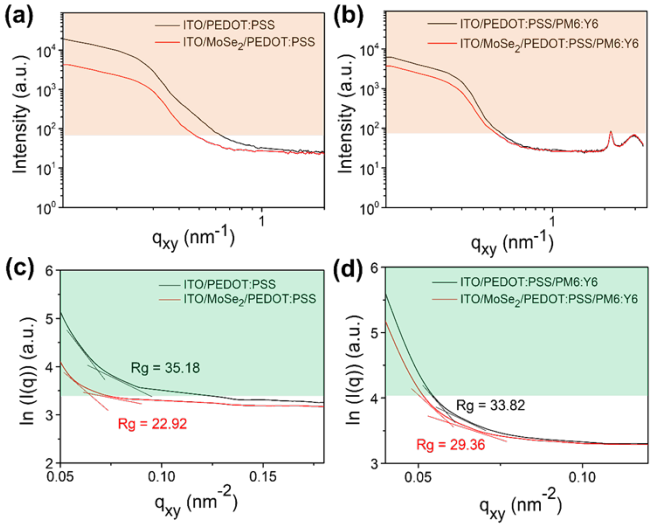

Fig. 6. GISAXS intensity profiles of (a) ITO/PEDOT:PSS and ITO/$MoSe_2$ QDs/PEDOT:PSS and (b) ITO/PEDOT:PSS/PM6:Y6 and ITO/$MoSe_2$ QDs/PEDOT:PSS/PM6:Y6 thin films along the IP directions. The Guinier approximation of GISAXS intensity profiles of (c) ITO/PEDOT:PSS and ITO/$MoSe_2$ QDs/PEDOT:PSS and (d) ITO/PEDOT:PSS/PM6:Y6 and ITO/$MoSe_2$ QDs/PEDOT:PSS/PM6:Y6 in low-*q* region.

In order to further investigate the effect of $MoSe_2$ QDs on mesoscopic structure, the grazing incidence small-angle X-ray scattering (GISAXS) of PEDOT:PSS and PM6:Y6 thin films with and without $MoSe_2$ QDs were determined. Fig. S10a and S10b presents the 2D GISAXS images of HEL and active layer with and without $MoSe_2$ QDs, respectively. From these scattering images, the Yoneda peak with a high intensity peak along the IP direction can be observed.[69] The corresponding 1D IP profiles are shown in Fig. 6a and 6b and no obvious scattering peak is detected along the IP direction, indicating the nanostructure of PEDOT:PSS was less ordered along the q_{xy} direction.[70] Fig. S10c and S10d show the 2D GISAXS images of the active layers with and without $MoSe_2$ QDs. It is clear that the scattering peaks were seen along the OOP direction, implying that the PM6:Y6 thin films form a layered structure.[71] It is believed that the domain size is another key impact factor for the performance of OSCs. The radius of gyration (R_g) of the clusters of the PEDOT:PSS and PM6:Y6 thin films with and without $MoSe_2$ QDs is quantitatively calculated by Guinier approximation according to the following equation:[72,73]

$$I\left(q_{xy}\right)=I(0)\exp\left(-\frac{q_{xy}^2R_g^2}{3}\right) \quad (2)$$

where $I(q_{xy})$ and $I(0)$ are the scattering intensity and the zero-angle scattering intensity, q_{xy} is obtained by $4\pi \sin(\frac{\theta}{2})/\lambda$, θ is the scattering angle and λ is the wavelength of incidence light. So, R_g is the average of the absolute values of two slopes ($lnI(q_{xy})$ *vs* q_{xy}^2) in the low-*q* region (ca. 0.05–0.13 nm^{-1}). From Fig. 6c and 6d, the R_g of PEDOT:PSS, $MoSe_2$ QDs/PEDOT:PSS, PEDOT:PSS/PM6:Y6 and $MoSe_2$ QDs/PEDOT:PSS/PM6:Y6 thin films are calculated to be 35.18, 22.92, 33.82 and 29.36 nm, respectively, indicating that the insertion of $MoSe_2$ QDs contributes to the reduction of domain sizes and phase separation of both PEDOT:PSS and PM6:Y6.

It is well established that stability is an important factor for practical application of OSCs.[74] To evaluate the stability of our OSCs, the performances in air of the control cell and the champion cell based on $MoSe_2$ QDs-6000r/PEDOT:PSS after simple encapsulation are measured as shown in Fig. S11. It can be seen distinctly that the PCE based on $MoSe_2$ QDs/PEDOT:PSS composite HEL can maintain 85% PCE after 120 h, which is superior to the control cell (67%). The better long-term stability is ascribed to the insertion of $MoSe_2$ QDs which can alleviate the large area contact of ITO and active layer with PSS.

To demonstrate the universality of the strategy as discussed in this work for performance optimization of OSCs, we also applied $MoSe_2$ QDs/PEDOT:PSS composite HEL into other nonfullerene and fullerene-based systems, namely, PBDB-T/ITIC, PTB7-Th/$PC_{71}BM$, and P3HT/$PC_{61}BM$. The device performances of these OSCs are plotted in Fig. S12 and S13. It can be found that, the insertion of $MoSe_2$ QDs leads to PCE improvement from 9.51% to 10.41%, 7.88% to 8.32%, and 2.93% to 3.24%, respectively, for the PBDB-T/ITIC, PTB7-Th/$PC_{71}BM$, and P3HT/$PC_{61}BM$-based cells. Detailed photovoltaic parameters are listed in Table S7. The similar performance enhancement in other systems demonstrates that introducing $MoSe_2$ QDs/PEDOT:PSS as bilayer HEL is an effective pathway for the optimization of OSCs.

Conclusions

To conclude, $MoSe_2$ QDs were synthesized by a lithium intercalation method and utilized as a modifier in HEL for the optimization of OSCs. We found that high temperature annealing of thin film of $MoSe_2$ QDs led to the generation of O-Mo-Se band due to participated lattice oxygen which partially fill the Se vacancies and passivate the structural defects, as well as the formation of MoO_3 species. Meanwhile, we also learnt that the insertion of $MoSe_2$ QDs can induce the phase separation of PEDOT and PSS, and thus weaken the shield effect of PSS on PEDOT and improve the electron conductivity and WF of PEDOT:PSS. The device characterization results show that, BHJ solar cell based on $MoSe_2$ QDs/PEDOT:PSS composite HEL in PM6:Y6 and SZ2:N3 system yielded a maximum PCE of 16.08 and 17.08%, respectively, which are significantly higher than the control cell based on PEDOT:PSS (15.48 and 16.53%). These remarkable efficiencies in our work are the highest value among single junction solar cells with 2D materials as the interface modifier so far. The enhancement of device performances is mainly attributed to the improved hole transport ability and WF of HEL, increased exciton dissociation and charge extraction probability at the electrode/function layer interface, as well as reduced charge recombination due to the better phase

separation of PEDOT and PSS and active layer as a result of introduction of $MoSe_2$ QDs interlayer. Moreover, the stability of OSCs with $MoSe_2$ QDs is improved remarkably because $MoSe_2$ QDs interlayer can prevent PEDOT:PSS from corroding the ITO electrode and remove the partial PSS from the interface of HEL and active layer. All these factors work synergistically and result in a significant enhancement of device performance. This strategy is also adaptable in other OSC systems, which therefore opens a new pathway for the application of TMD materials as interfacial modifiers in the 3rd generation of OSCs.

Author Contributions

Hong Lian and **Mingao Pan** fabricated the solar cell devices and optimized their processing parameters for photovoltaic performance. **Jinba Han** produced and characterized the $MoSe_2$ QDs. **Xiaozhe Cheng** performed subsequent stability tests with the help of **Hong Lian**. **Jiaen Liang** synthesized the SZ2 material. **Bin Wei** and **Qingchen Dong** supervised the materials synthesis and device fabrication. **Wenqiang Hua** conducted the GIWAXS measurements and analysis. **Yongquan Qu** performed the UPS and XPS measurements and analysis. **Yucheng Wu** provided discussion and suggestions. The manuscript was written by **Hong Lian, Qingchen Dong** and **He Yan**. The project was planned, directed and supervised by **Qingchen Dong**, **He Yan** and **Wai-Yeung Wong**. All authors discussed the results and commented on the manuscript.

Conflicts of interest

The authors declare that they have no known competing financial interests or personal relationships that could have appeared to influence the work reported in this paper.

Acknowledgements

We acknowledge the financial support from the National Natural Science Foundation of China (Grant No.: 61774109). This work was also supported by the Youth “Sanjin” Scholar Program, the Key R&D Project of Shanxi Province (International cooperation program, No. 201603D421032), and the Natural Science Foundation of Shanxi Province (Grant No.: 201801D211007). W.-Y.W. thanks the RGC Senior Research Fellowship Scheme (SRFS2021-5S01), the Hong Kong Polytechnic University (1-ZE1C), Research Institute for Smart Energy (CDA2) and the Endowed Professorship in Energy from Ms Clarea Au (847S). We acknowledge the beamline BL16B1 at Shanghai Synchrotron Radiation Facility for providing beam time.

References

1. Y. Lin, C. Cai, Y. Zhang, W. Zheng, J. Yang, E. Wang and L. Hou, *J. Mater. Chem. A*, 2017, **5**, 4093-4102.
2. F. Zhao, S. Dai, Y. Wu, Q. Zhang, J. Wang, L. Jiang, Q. Ling, Z. Wei, W. Ma, W. You, C. Wang and X. Zhan, *Adv. Mater.*, 2017, **29**, 1700144.
3. Z. Li, K. Jiang, G. Yang, J. Y. L. Lai, T. Ma, J. Zhao, W. Ma and H. Yan, *Nat. Commun.*, 2016, **7**, 13094.
4. Y. Lin, J. Wang, Z.-G. Zhang, H. Bai, Y. Li, D. Zhu and X. Zhan, *Adv. Mater.* 2015, **27**, 1170-1174.
5. J. Hou, O. Inganäs, R. H. Friend and F. Gao, *Nat. Mater.*, 2018, **17**, 119-128.
6. S. Li, L. Zhan, F. Liu, J. Ren, M. Shi, C.-Z. Li, T. P. Russell and H. Chen, *Adv. Mater.*, 2018, **30**, 1705208.
7. J. Yuan, Y. Zhang, L. Zhou, G. Zhang, H.-L. Yip, T.-K. Lau, X. Lu, C. Zhu, H. Peng, P. A. Johnson, M. Leclerc, Y. Cao, J. Ulanski, Y. Li and Y. Zou, *Joule*, 2019, **3**, 1140-1151.
8. L. Meng, Y. Zhang, X. Wan, C. Li, X. Zhang, Y. Wang, X. Ke, Z. Xiao, L. Ding, R. Xia, H.-L. Yip, Y. Cao and Y. Chen, *Science*, 2018, **361**, 1094-1098.
9. H.-L. Yip and A. K. Y. Jen, *Energy Environ. Sci.*, 2012, **5**, 5994-6011.
10. B. Xu and J. Hou, *Adv. Energy Mater.*, 2018, **8**, 1800022.
11. K. H. Park, Y. An, S. Jung, H. Park and C. Yang, *ACS Nano*, 2017, **11**, 7409-7415.
12. Q. Xie, J. Zhang, H. Xu, X. Liao, Y. Chen, Y. Li and L. Chen, *Org. Electron.*, 2018, **61**, 207-214.
13. H. Xu, F. Yuan, D. Zhou, X. Liao, L. Chen and Y. Chen, *J. Mater. Chem. A*, 2020, **8**, 11478-11492.
14. H. Xu, H. Zou, D. Zhou, G. Zeng, L. Chen, X. Liao and Y. Chen, *ACS Appl. Mater. Interfaces*, 2020, **12**, 52028-52037.
15. X. Yu, T. J. Marks and A. Facchetti, *Nat. Mater.*, 2016, **15**, 383-396.
16. K.-G. Lim, S. Ahn, Y.-H. Kim, Y. Qi and T.-W. Lee, *Energy Environ. Sci.*, 2016, **9**, 932-939.
17. L. Wang, S. Guo, K. Zhou and W. Ma, *Sustainable Energy Fuels*, 2020, **4**, 4934-4955.
18. M. P. d. Jong, L. J. v. IJzendoorn and M. J. A. d. Voigt, *Appl. Phys. Lett.*, 2000, **77**, 2255-2257.
19. Y. Sun, C. J. Takacs, S. R. Cowan, J. H. Seo, X. Gong, A. Roy and A. J. Heeger, *Adv. Mater.*, 2011, **23**, 2226-2230.
20. T. Yang, M. Wang, F. Jia, X. Ren and G. Gao, *J. Mater. Chem. C*, 2020, **8**, 2326-2335.
21. J. Meyer, S. Hamwi, M. Kröger, W. Kowalsky, T. Riedl and A. Kahn, *Adv. Mater.*, 2012, **24**, 5408-5427.
22. Y.-J. Lee, J. Yi, G. F. Gao, H. Koerner, K. Park, J. Wang, K. Luo, R. A. Vaia and J. W. P. Hsu, *Adv. Energy Mater.*, 2012, **2**, 1193-1197.
23. H. Zhang, J. Cheng, F. Lin, H. He, J. Mao, K. S. Wong, A. K. Y. Jen and W. C. H. Choy, *ACS Nano*, 2016, **10**, 1503-1511.
24. Z. Zheng, Q. Hu, S. Zhang, D. Zhang, J. Wang, S. Xie, R. Wang, Y. Qin, W. Li, L. Hong, N. Liang, F. Liu, Y. Zhang, Z. Wei, Z. Tang, T. P. Russell, J. Hou and H. Zhou, *Adv. Mater.*, 2018, **30**, 1801801.
25. Z. Yin, J. Wei and Q. Zheng, *Adv. Sci.*, 2016, **3**, 1500362.
26. C. Tan, X. Cao, X.-J. Wu, Q. He, J. Yang, X. Zhang, J. Chen, W. Zhao, S. Han, G.-H. Nam, M. Sindoro and H. Zhang, *Chem. Rev.*, 2017, **117**, 6225-6331.
27. G. Tang, P. You, Q. Tai, A. Yang, J. Cao, F. Zheng, Z. Zhou, J. Zhao, P. K. L. Chan and F. Yan, *Adv. Mater.*, 2019, **31**, 1807689.
28. Q. V. Le, T. P. Nguyen and S. Y. Kim, *Phys. Status Solidi RRL.*, 2014, **8**, 390-394.
29. W. Xing, Y. Chen, X. Wang, L. Lv, X. Ouyang, Z. Ge and H. Huang, *ACS Appl. Mater. Interfaces*, 2016, **8**, 26916-26923.
30. S. Das, D. Pandey, J. Thomas and T. Roy, *Adv. Mater.*, 2019,

31, 1802722.
31. Z. Yuan, Z. Wu, S. Bai, W. Cui, J. Liu, T. Song and B. Sun, *Org. Electron.*, 2015, **26**, 327-333.
32. Q. Van Le, T. P. Nguyen, M. Park, W. Sohn, H. W. Jang and S. Y. Kim, *Adv. Opt. Mater.*, 2016, **4**, 1796-1804.
33. X. Gu, W. Cui, H. Li, Z. Wu, Z. Zeng, S.-T. Lee, H. Zhang and B. Sun, *Adv. Energy Mater.*, 2013, **3**, 1262-1268.
34. X. Gu, W. Cui, T. Song, C. Liu, X. Shi, S. Wang and B. Sun, *ChemSusChem*, 2014, **7**, 416-420.
35. Q. V. Le, T. P. Nguyen, H. W. Jang and S. Y. Kim, Phys. *Chem. Chem. Phys.*, 2014, **16**, 13123-13128.
36. X. Zhang, Z. Lai, Z. Liu, C. Tan, Y. Huang, B. Li, M. Zhao, L. Xie, W. Huang and H. Zhang, *Angew. Chem. Int. Ed.,* 2015, **54**, 5425-5428.
37. K. C. Kwon, C. Kim, Q. V. Le, S. Gim, J.-M. Jeon, J. Y. Ham, J.-L. Lee, H. W. Jang and S. Y. Kim, *ACS Nano*, 2015, **9**, 4146-4155.
38. J.-M. Yun, Y.-J. Noh, J.-S. Yeo, Y.-J. Go, S.-I. Na, H.-G. Jeong, J. Kim, S. Lee, S.-S. Kim, H. Y. Koo, T.-W. Kim and D.-Y. Kim, *J. Mater. Chem. C*, 2013, **1**, 3777-3783.
39. P. Ge, H. Hou, C. E. Banks, C. W. Foster, S. Li, Y. Zhang, J. He, C. Zhang and X. Ji, *Energy Storage Mater.*, 2018, **12**, 310-323.
40. Q. Su, X. Cao, T. Yu, X. Kong, Y. Wang, J. Chen, J. Lin, X. Xie, S. Liang and A. Pan, *J. Mater. Chem. A*, 2019, **7**, 2871-22878.
41. J. Wang, H. Yu, C. Hou and J. Zhang, *Solar RRL*, 2020, **4**, 1900428.
42. K. S. Lee, Y. J. Park, J. Shim, C.-H. Lee, G.-H. Lim, H. Y. Kim, J. W. Choi, C.-L. Lee, Y. Jin, K. Yu, H.-S. Chung, B. Angadi, S.-I. Na and D. I. Son, *J. Mater. Chem. A*, 2019, **7**, 15356-15363.
43. H. Liu, J. Peng, W. Liu, Y. Wang, J. Wu, G. Zhang, X. Wang and Y. Yan, *NPG Asia Mater.*, 2018, **10**, 309-317.
44. T. Yan, W. Song, J. Huang, R. Peng, L. Huang and Z. Ge, *Adv. Mater.*, 2019, **31**, 1902210.
45. J. Wang, Z. Zheng, D. Zhang, J. Zhang, J. Zhou, J. Liu, S. Xie, Y. Zhao, Y. Zhang, Z. Wei, J. Hou, Z. Tang and H. Zhou, *Adv. Mater.*, 2019, **31**, 1806921.
46. Z. Ling, Y. Zhao, S. Wang, S. Pan, H. Lian, C. Peng, X. Yang, Y. Liao, W. Lan, B. Wei and G. Chen, *J. Mater. Chem. C*, 2019, **7**, 9354-9361.
47. T. Yan, J. Ge, T. Lei, W. Zhang, W. Song, B. Fanady, D. Zhang, S. Chen, R. Peng and Z. Ge, *J. Mater. Chem. A*, 2019, **7**, 25894-25899.
48. J. Liang, M. Pan, G. Chai, Z. Peng, J. Zhang, S. Luo, Q. Han, Y. Chen, A. Shang, F. Bai, Y. Xu, H. Yu, J. Y. L. Lai, Q. Chen, M. Zhang, H. Ade and H. Yan, *Adv. Mater. 2020, **32**, 2003500.*
49. P. Qin, G. Fang, W. Ke, F. Cheng, Q. Zheng, J. Wan, H. Lei and X. Zhao, *J. Mater. Chem. A,* 2014, **2**, 2742-2756.
50. Y. Wang, J. Li, T. Li, J. Wang, K. Liu, Q. Jiang, J. Tang and X. Zhan, *Small*, 2019, **15**, 1903977.
51. J.-M. Yun, Y.-J. Noh, C.-H. Lee, S.-I. Na, S. Lee, S. M. Jo, H.-I. Joh and D.-Y. Kim, *Small*, 2014, **10**, 2319-2324.
52. Y. Lin, B. Adilbekova, Y. Firdaus, E. Yengel, H. Faber, M. Sajjad, X. Zheng, E. Yarali, A. Seitkhan, O. M. Bakr, A. El-Labban, U. Schwingenschlögl, V. Tung, I. McCulloch, F. Laquai and T. D. Anthopoulos, *Adv. Mater.*, 2019, **31**, 1902965.
53. B. Liu, Y. Wang, P. Chen, X. Zhang, H. Sun, Y. Tang, Q. Liao, J. Huang, H. Wang, H. Meng and X. Guo, *ACS Appl. Mater. Interfaces*, 2019, **11**, 33505-33514.
54. C. Huang and H. Yu, *ACS Appl. Mater. Interfaces*, 2020, **12**, 19643-19654.
55. F. Pan, C. Sun, Y. Li, D. Tang, Y. Zou, X. Li, S. Bai, X. Wei, M. Lv, X. Chen and Y. Li, *Energy Environ. Sci.*, 2019, **12**, 3400-3411.
56. G. Ma, Z. Liu and N. Wang, *Sol. Energy*, 2018, **170**, 164-173.
57. B. J. Leever, C. A. Bailey, T. J. Marks, M. C. Hersam and M. F. Durstock, *Adv. Energy Mater.*, 2012, **2**, 120-128.
58. B. Ecker, H.-J. Egelhaaf, R. Steim, J. Parisi and E. von Hauff, *J. Phys. Chem. C*, 2012, **116**, 16333-16337.
59. P. Anger, P. Bharadwaj and L. Novotny, *Phys. Rev. Lett.*, 2006, **96**, 113002.
60. M.-H. Lee, L. Chen, N. Li and F. Zhu, *J. Mater. Chem. C*, 2017, **5**, 10555-10561.
61. H. C. Lim, S. H. Min, E. Lee, J. Jang, S. H. Kim and J.-I. Hong, *ACS Appl. Mater. Interfaces*, 2015, **7**, 11069-11073.
62. J. Wang, H. Yu, C. Hou and J. Zhang, *ACS Appl. Mater. Interfaces*, 2020, **12**, 26543-26554.
63. Q. Yang, S. Yu, P. Fu, W. Yu, Y. Liu, X. Liu, Z. Feng, X. Guo and C. Li, *Adv. Funct. Mater.*, 2020, **30**, 1910205.
64. A. Hu, L. Tan, X. Hu, L. Hu, Q. Ai, X. Meng, L. Chen and Y. Chen, *J. Mater. Chem. C*, 2017, **5**, 382-389.
65. G. Zotti, S. Zecchin, G. Schiavon, F. Louwet, L. Groenendaal, X. Crispin, W. Osikowicz, W. Salaneck and M. Fahlman, *Macromolecules*, 2003, **36**, 3337-3344.
66. Y. Xia, H. Zhang and J. Ouyang, *J. Mater. Chem.*, 2010, **20**, 9740-9747.
67. Q. An, J. Wang, W. Gao, X. Ma, Z. Hu, J. Gao, C. Xu, M. Hao, X. Zhang, C. Yang and F. Zhang, *Sci. Bull.*, 2020, **65**, 538-545.
68. Y. Xiao and X. Lu, *Materials Today Nano*, 2019, **5**, 100030.
69. P. Müller-Buschbaum, *Adv. Mater.*, 2014, **26**, 7692-7709.
70. Q. Wei, M. Mukaida, Y. Naitoh and T. Ishida, *Adv. Mater.*, 2013, **25**, 2831-2836.
71. L. Zhu, M. Zhang, G. Zhou, T. Hao, J. Xu, J. Wang, C. Qiu, N. Prine, J. Ali, W. Feng, X. Gu, Z. Ma, Z. Tang, H. Zhu, L. Ying, Y. Zhang and F. Liu, *Adv. Energy Mater.*, 2020, **10**, 2070083.
72. P. Bi, T. Xiao, X. Yang, M. Niu, Z. Wen, K. Zhang, W. Qin, S. K. So, G. Lu, X. Hao and H. Liu, *Nano Energy*, 2018, **46**, 81-90.
73. P. Bi, F. Zheng, X. Yang, M. Niu, L. Feng, W. Qin and X. Hao, *J. Mater. Chem. A*, 2017, **5**, 12120-12130.
74. J. Yao, B. Qiu, Z.-G. Zhang, L. Xue, R. Wang, C. Zhang, S. Chen, Q. Zhou, C. Sun, C. Yang, M. Xiao, L. Meng and Y. Li, *Nat. Commun.*, 2020, **11**, 2726.